

Oil slick detection by SAR imagery using Support Vector Machines

Grégoire MERCIER* and Fanny GIRARD-ARDHUIN†‡

*GET/ENST Bretagne, dpt ITI,
TAMCIC, team TIME, CNRS UMR 2872,
Technopôle Brest-Iroise, CS 83818,
F-29 238 Brest Cedex, France.

†IFREMER DOPS/LOS,
Technopôle Brest-Iroise, BP 70,
F-29 280 Plouzané, France.

‡CNES,
2 place Maurice Quentin,
F-75 001 Paris, France.

Abstract— Spaceborne Synthetic Aperture Radar (SAR) is well adapted to detect ocean pollution independently from daily or weather condition. In fact, oil slicks have specific impact on ocean wave spectra. Initial wave spectra may be characterized by three kinds of waves, big, medium and small, which correspond physically to gravity and gravity-capillary waves. The increase of viscosity due to the presence of oil damps gravity-capillary waves. This induces a damping of the backscattering to the sensor, but also a damping of the energy of the wave spectra. Thus, local segmentation of wave spectra may help oil slick detection. It can be achieved by the segmentation of a multiscale decomposition of the original SAR image.

In this work, a supervised oil slick detection is proposed by using Support Vector Machines into the wavelet decomposition of a SAR image. It performs accurate detection with no consideration to signal stationarity nor to the presence of strong backscatters (such as ship). Moreover, when using normalized SAR images, the kernel expansion may be generalized from one image to another to make a near unsupervised detection scheme.

The algorithm has been applied on Envisat ASAR images. First experiments yield accurate segmentation results with a very limited number of false alarms.

I. INTRODUCTION

The oceanic sea surface is complex and often governed by non-linear dynamic systems. Surface waves, that are found in the ocean, range from the millimeter scale to hundreds of meters. By considering an infinite sea surface, the wind induces capillary waves by friction. Capillary waves cannot propagate and they vanish with the wind. But they transfer their energy to waves with a longer wavelength until they reach an equilibrium that depends on the wind. In addition, gravity waves transfer their energy to gravity-capillary waves. Several models have been proposed to characterize the sea surface spectrum with an accuracy that depends on the wavelength bandwidth. Those models integrate the wind, but also the current, atmospheric pressure and so on. An interesting comparison of some models may be found in [1] in the context of SAR imagery. On the one hand, capillary waves are generated by friction, and more specifically by friction velocity, related by wind speed and surface properties, which die down when the friction decreases. On the other, gravity waves are generated indirectly

by sea spectrum energy spreading and propagating over long distances far from their origins.

The next paragraphs will show that backscattering phenomena are directed by gravity-capillary waves (due to the wavelength of electromagnetic waves) while typical SAR systems are sensitive to gravity waves (due to their resolution).

A. Historical point of view

In the beginning of the first century, Pline the Old observed natural slicks and their effects on the sea surface: the waves damping. From the 18th century, scientists tried to find theories. Benjamin Franklin [2] is the first to be interested in the phenomena. Afterwards, many scientists were involved in this topic. In 1882, an experimental demonstration conducted by John Shields in Peterhead (U.K.) proves the efficiency of the phenomena of waves damping by dumping oil in the harbor to protect boats during a storm. Then, governments encourage many experiments. Without being understood, this effect has been used to save boats during storms tipping out oil to break waves [3, 4], notably in U.S., English and French Navy. After Franklin's first researches, Marangoni explained that capillary wave damping is function of slick elasticity [5–7]. This theory was followed by Rayleigh, Aitken and Reynolds among others but Marangoni's is still considered as the reference.

When gravity-capillary waves propagate, their successive compressions and extensions increase dissipation. When a slick covers the surface, wind has less effect on the surface, the amplitude of wave crest/trough decreases, implying a surface stress gradient, with opposite strength to this alternated motion. The Marangoni waves are created when a stress gradient exists, *i.e.* with visco-elastic slick. The Marangoni wave is partly longitudinal in the upper layer where dissipation is attenuated and partly tangential linked to stress gradient associated with visco-elastic slick properties [6]. Visco-elastic surfaces only carry two kinds of waves: gravity-capillary waves and Marangoni waves. The high frequency waves damping is maximum when these two kinds of waves are in resonance. The surface waves damping is linked to surface stress decrease, which is mostly associated with slick elasticity,

but also with oil nature, density and surface viscosity [8–10]. Elasticity stabilizes the surface and avoids wind-wave generation.

Waves can be considered through their energy, composed of three terms: wind energy, wave-wave non-linear energy transfer and dissipation. It is expected that the two first parts are modified by slicks, but the third one is changed as well: the damping of the longest and the shortest waves suggests that non-linear interactions are important [7]. While short wave energy is reduced by slick, viscosity dissipation spread energy by non-linear transfer to higher and smaller frequencies.

A slick at the ocean surface damps waves, implying an energy decrease by distribution to high and short waves, and a spectral peak shift corresponding to the important surface stress decrease.

B. Sea surface observation with SAR data

Radar electromagnetic waves are backscattered by the sea surface. The simplest model that describes this backscattering process is the Bragg resonance effect that links the sea surface and electromagnetic wavelengths. According to this model, the sea surface waves of wavenumber $\kappa_{\text{sea}} = 2\kappa_{\text{SAR}} \sin \theta$ contribute to the scattering process (κ_{SAR} being the wavenumber of the electromagnetic wave and θ the incidence angle).

More precisely, most SAR sensors that are used on civil satellites use the C band (*i.e.* a wavelength of about 5.6 cm). By considering incidence angles from 15 to 45° according to the sensors and their acquisition modes, gravity-capillary waves of wavelengths from 4 to 14 cm intervene in the scattering process.

Nevertheless, SAR image resolution is much larger than the wavelength and the sensor is sensitive to large scale oceanographic phenomena. In fact, the Bragg mechanism considers waves of one wavelength only [11] while it is necessary to consider a bandwidth or, even better, the overall wave spectrum. Moreover, wave motion induces specific modulation on the wave spectrum acquired by the SAR sensor. Hence, surface roughness induced by short waves is modulated by longer waves allowing SAR imagery to characterize “indirectly” oceanophysical phenomena such as swell, internal waves, coastal bathymetry or oil slicks.

C. Usual strategy for oil spill detection

A viscous area is seen smoother than a clean sea surface since small wave generation and propagation is stopped by the viscosity of a slick. From the SAR sensor point of view, a slick is characterized by a lack of backscattered energy and then restituted through a dark area [12]. According to the Bragg phenomenon, the backscattering process is mostly due to surface roughness.

That is why many slick detection algorithms are based on a thresholding technique [13–15]. Nevertheless, this process is not efficient when:

- the wind is increasing (basically over 10-14 m/s);
- the sea state is different (more precisely its wave spectrum shape);

- viscoelastic oil properties are different (different kinds of oil but also their degradation);
- possible bad-detection with look-alikes (*e.g.* weak wind area, upwelling, phytoplankton, algae, etc.).

Moreover, a radiometric point of view shows some limitations since wave slopes that are not oriented to the sensor are restituted with a lower radiometry that may be confused with small slicks. That is why most slick detection strategies include a post-processing stage to remove small slicks through geometrical, morphological or contextual criteria [16–18].

D. Multiscale strategy

A priori, the proposed multiscale strategy that is implemented to detect oil slicks may be justified by several concepts mentioned above:

- the SAR sensor is only sensitive to surface roughness (at a centimeter scale) which is modulated by larger scale phenomena that induce shades of texture;
- the increase of viscosity, due to the presence of an oil slick on the sea surface, affects the sea surface wave spectrum shape;
- oil slicks induce dark areas on the SAR images under certain conditions, such as a limited wind (*i.e.* under 10-14 m/s).

The paper is organized as follows: section II presents the multiscale transformation and explains how the initial sea surface observation is represented as coarse radiometric information associated with a set of coefficients linked to the surface roughness at several scales. It shows that the multiscale transformation is an appropriate tool for the local characterization of wave spectrum shape. Section III presents the concept of segmentation by Support Vectors, while section IV focuses on the use of kernels to assess the sea surface wave spectrum segmentation. Section V shows some results of oil slick detection from ENVISAT ASAR images with a difficult case found during the Prestige pollution drift. Section VI concludes and gives some perspectives.

II. MULTISCALE REPRESENTATION

A. Multiscale wavelet transform

The decomposition is implemented in order to analyze the local shape of the sea surface wave spectrum. Then, a shift invariant multiscale differential operator is used to characterize the sharp structures of a signal f [19]. The wavelet operator is then defined (in 1D) as:

$$\mathcal{W}_\ell \{f\} (b, a) = a^\ell \frac{\partial^\ell}{\partial b^\ell} (f * \overline{\theta}_a) (b),$$

where ℓ is the decomposition level ($0 \leq \ell < L$). Convolution $f * \overline{\theta}_a$ acts as a smooth of f over a domain a ; $\overline{\theta}_a(x) = \frac{1}{\sqrt{a}} \theta\left(-\frac{x}{a}\right)$.

When considering the first derivatives, the modulus of $\mathcal{W}_1 \{f\} (b, a) = a \frac{\partial}{\partial b} (f * \overline{\theta}_a) (b)$ is maximum where $(f * \overline{\theta}_a) (b)$ fluctuates. When considering the second derivative, the modulus maxima of $\mathcal{W}_2 \{f\} (b, a) = a^2 \frac{\partial^2}{\partial b^2} (f * \overline{\theta}_a) (b)$ is maximum where $(f * \overline{\theta}_a) (b)$ fluctuates.

$\overline{\theta_a}(b)$ correspond to the points of maximum curvature of f . More generally, wavelet coefficients are proportional to the components of the gradient of f smoothed by θ_a . Then, with such a multiscale differential operator each singularity of f is detected by following the modulus maxima of the wavelet coefficients towards finer scales. Moreover, it has been shown that if f adopts a band-limited Fourier transform and if the wavelet ($\psi = -\frac{\partial \theta}{\partial x}$) has compact support, then the wavelet modulus maxima define a complete and stable signal representation [20].

In order to analyze the sea surface wave spectrum shape yielded by a SAR observation, a wavelet-based multiscale edge detector is defined as a 2D separable dyadic wavelet. Its Fourier transforms, noted as $\tilde{X}(\omega) = \text{FT}\{x(t)\}$, may be written (in 2D) as:

$$\begin{aligned}\tilde{\Psi}^{\text{hori}}(\omega_{\text{hori}}, \omega_{\text{vert}}) &= \tilde{G}\left(\frac{\omega_{\text{hori}}}{2}\right) \tilde{\Phi}\left(\frac{\omega_{\text{hori}}}{2}\right) \tilde{\Phi}\left(\frac{\omega_{\text{vert}}}{2}\right) \\ \tilde{\Psi}^{\text{vert}}(\omega_{\text{hori}}, \omega_{\text{vert}}) &= \tilde{G}\left(\frac{\omega_{\text{vert}}}{2}\right) \tilde{\Phi}\left(\frac{\omega_{\text{hori}}}{2}\right) \tilde{\Phi}\left(\frac{\omega_{\text{vert}}}{2}\right) \\ \text{with } \tilde{\Phi}(\omega) &= \left(\frac{\sin \frac{\omega}{2}}{\frac{\omega}{2}}\right)^{m+1} e^{-j\varepsilon \frac{\omega}{2}}, \\ \varepsilon &= \begin{cases} 1 & m \text{ even} \\ 0 & m \text{ odd.} \end{cases}\end{aligned}$$

This yields low-pass filter coefficients $\tilde{H}(\omega) = \sqrt{2} \left(\cos \frac{\omega}{2}\right)^{m+1} e^{-j\varepsilon \frac{\omega}{2}}$ that correspond to a box-spline of degree m . The function $g(\cdot)$ is a discrete approximation of the derivative operator, of Fourier transform: $\tilde{G}(\omega) = -j\sqrt{2} \left(\sin \frac{\omega}{2}\right)^{m+1} e^{-j\varepsilon \frac{\omega}{2}}$.

B. Mother wavelet design

In order to analyze the sea surface wave spectrum as locally as possible, a scale function $\theta(\cdot)$ was chosen as short as possible and its Fourier transform is a cubic spline. The multiscale decomposition gives a set of images for which the wavelet coefficients represent the details at a coarser and coarser scale ℓ ($0 \leq \ell < L$), associated with a smooth image which is a coarse radiometric approximation (at scale L) of the original image.

Then, a SAR image $I(x, y)$ may be represented with its details at different scales by:

$$I \longrightarrow \begin{cases} I_L^{\text{low}} &= I(x, y) * \theta(2^{-(L-1)}x, 2^{-(L-1)}y) \\ I_\ell^{\text{hori}} &= I(x, y) * \psi^{\text{hori}}(2^{-\ell}x, 2^{-\ell}y) \\ I_\ell^{\text{vert}} &= I(x, y) * \psi^{\text{vert}}(2^{-\ell}x, 2^{-\ell}y) \end{cases}$$

which corresponds to cutting the Fourier spectrum into a dyadic sequence: $\omega_{\text{max}}/2^{\ell+1}$, $0 \leq \ell < L$.

Note that the vector $(I_\ell^{\text{hori}}, I_\ell^{\text{vert}})^t$ is proportional to the gradient of I smoothed by θ_{2^ℓ} . In this kind of decomposition, there is no diagonal decomposition as is the case in most dyadic multiresolution decompositions, since this decomposition acts as a multiscale edge detector. When applied to SAR images, it is not necessary to use more than three or four levels since $I_{L=3}^{\text{low}}$ contains details at the swell scale for ASAR wide mode products, which is enough for our application.

III. THE SVM APPROACH

The complete mathematical formulation of SVM can be found in [21, 22]. We just give a brief description of the classification process.

A. SVM basis

A two-class classification problem can be stated the following way: N training sample are available and can be represented by the set pairs $\{(y_i, \mathbf{x}_i), i = 1, 2, \dots, N\}$ with y_i a class label of value ± 1 and $\mathbf{x}_i \in \mathbb{R}^n$ feature vector with n components. The classifier is represented by the function $f(\mathbf{x}; \boldsymbol{\alpha}) \rightarrow y$ with $\boldsymbol{\alpha}$ the parameters of the classifier.

The SVM method consist in finding the optimum separating hyperplan so that:

- 1) Samples with labels $y = \pm 1$ are located on each side of the hyperplane;
- 2) The distance of the closest vectors to the hyperplane in each side of maximum. These are called support vectors and the distance is the optimal margin (see Fig. 1-a-).

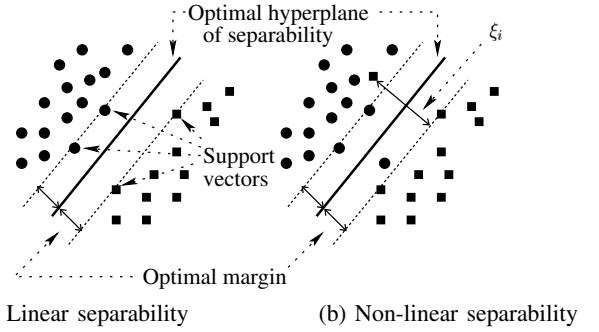


Fig. 1. SVM classifier.

The hyperplane is defined by $\langle \mathbf{w}, \mathbf{x} \rangle + b = 0$ where (\mathbf{w}, b) are the parameters of the hyperplane. The vectors that are not on this hyperplane lead to: $\langle \mathbf{w}, \mathbf{x} \rangle + b \geq 0$ and allow the classifier to be defined as: $f(\mathbf{x}; \boldsymbol{\alpha}) = \text{sgn}(\langle \mathbf{w}, \mathbf{x} \rangle + b)$. The support vectors lie on two hyperplanes, which are parallel to the optimal hyperplane, of equation: $\langle \mathbf{w}, \mathbf{x} \rangle + b = \pm 1$.

The maximization of the margin with the equations of the two support vector hyperplanes leads to the following constrained optimization problem:

$$\min \left\{ \frac{1}{2} \|\mathbf{w}\|^2 \right\} \text{ with } y_i (\langle \mathbf{w}, \mathbf{x}_i \rangle + b) \geq 1, i = 1, \dots, N. \quad (1)$$

B. Non-linear separability

If the training samples are not linearly separable (see Fig. 1-b-), a regularization parameter C and error variables ε_i are introduced in (1) in order to reduce the weighting of misclassified vectors.

This optimization problem can be solved using Lagrange

multipliers and then becomes:

$$\left\{ \begin{array}{l} \min \left\{ \sum_{i=1}^N \lambda_i - \frac{1}{2} \sum_{i,j=1}^N \lambda_i \lambda_j y_i y_j \langle \mathbf{x}_i, \mathbf{x}_j \rangle \right\}, \\ 0 \leq \lambda_i \leq C, \quad \forall i = 1, 2, \dots, N, \\ \sum_{i=1}^N \lambda_i y_i = 0, \quad \forall i = 1, 2, \dots, N, \end{array} \right. \quad (2)$$

where the λ_i are the Lagrangian multipliers and are non-zero only for the support vectors. Thus, hyperplane parameters (\mathbf{w}, b) and the classifier function $f(\mathbf{x}; \mathbf{w}, b)$ can be computed by optimization process [23].

C. Multiple class separation

SVM are designed to solve two-class problems. The *one against one* technique is used for M -class segmentation. $\frac{M(M-1)}{2}$ classifiers are applied on each pair of classes, the most often computed label is kept for each vector.

IV. KERNEL-BASED SVM

A. Non-linear classifier

SVM can be generalized to compute nonlinear decision surfaces in \mathbb{R}^n and to take an appropriate point of view onto the feature space. The method consists in projecting the data in a higher dimension space where they are considered to become linearly separable. SVM applied in this space lead to the determination of nonlinear surfaces in the original space. Actually, the projection can be simulated using a kernel method.

It can be noticed that only dot products $\langle \mathbf{x}_i, \mathbf{x}_j \rangle$ are involved in (2). If $\mathbf{x} \in \mathbb{R}^n$ is projected into a higher-dimension space \mathcal{H} with a non-linear function $\Phi : \mathbb{R}^n \rightarrow \mathcal{H}$, then $\langle \mathbf{x}_i, \mathbf{x}_j \rangle$ is replaced by $\langle \Phi(\mathbf{x}_i), \Phi(\mathbf{x}_j) \rangle$. The kernel function $K(\mathbf{x}_i, \mathbf{x}_j) = \langle \Phi(\mathbf{x}_i), \Phi(\mathbf{x}_j) \rangle$ is introduced in (2) and do not require explicit knowledge of $\Phi(\cdot)$.

Then, the non-linear classifier can be expressed as:

$$f(\mathbf{x}; \alpha) = \text{sgn} \left(\sum_{i=1}^{N_S} \lambda_i y_i K(\mathbf{s}_i, \mathbf{x}) + b \right), \quad (3)$$

where the \mathbf{s}_i are the N_S support vectors.

B. Usual kernels

Every function $K(\cdot, \cdot)$ that satisfies Mercer's conditions may be considered as an eligible kernel. The Mercer's conditions state as:

$$\forall g(\cdot) \in \mathcal{L}^2(\mathbb{R}^n) \quad \text{so that} \quad \int g(\mathbf{x})^2 d\mathbf{x} \text{ is finite,} \\ \text{then} \quad \int K(\mathbf{x}, \mathbf{y}) g(\mathbf{x}) g(\mathbf{y}) d\mathbf{x} d\mathbf{y} \geq 0. \quad (4)$$

For oil slick segmentation, we observed that polynomial, eq. (5), or sigmoid kernels, eq. (6), were the more satisfactory since there minimize the number of false alarms:

$$K_{\text{Polynomial}}(\mathbf{x}, \mathbf{s}_i) = (\langle \mathbf{x}, \mathbf{s}_i \rangle + 1)^p, \quad (5)$$

$$K_{\text{Sigmoid}}(\mathbf{x}, \mathbf{s}_i) = \tanh(\langle \mathbf{x}, \mathbf{s}_i \rangle + 1). \quad (6)$$

C. Texture kernels

It is of interest to consider not only pointwise observations through vector-to-vector comparisons but also local neighbourhoods to perform the local characterization of the sea surface wave spectra. A texture-based kernel has been developed in order to act as a contrast measurement of local texture on each component of the vectors.

Let's consider the neighbourhood of each component of vectors \mathbf{x} and \mathbf{y} . In this study, each component of vectors for the SVM approach are wavelet coefficients. Furthermore the neighbourhood concept is to be understood as a spatial neighbourhood on the image (on the sea surface) and not as a Voronoï cell in the \mathbb{R}^n or the \mathcal{H} space.

The wavelet coefficients distribution may be modelized by Alpha-stable process, generalized Gaussian or even Gaussian distributions. For accuracy of local parameter estimation, local probability density functions (pdf) have been chosen to follow the Gaussian law that is supposed to independent from a component to an other. Distributions are compared through the Bhattacharyya distance.

Thus, the texture kernel may be defined, as a polynomial kernel, as:

$$K(\mathbf{x}, \mathbf{y}) = (\mathcal{B}(p_{\mathbf{x}}, p_{\mathbf{y}}) + 1)^p, \\ = \left(\prod_{\ell=0}^{L-1} \int \sqrt{p_{x_\ell}(u) p_{y_\ell}(u)} du + 1 \right)^p. \quad (7)$$

D. Mixture of kernels

It is of interest to consider the backscattering process but also its local shape. Then, linear mixture of kernels can fit the dual point of view: similarity according to the dot product or euclidian distance and also, similarity according to the texture. Mixture of kernels may be defined as [24]:

$$K(\mathbf{x}, \mathbf{x}_i) = \mu K_a(\mathbf{x}, \mathbf{x}_i) + (1 - \mu) K_b(\mathbf{x}, \mathbf{x}_i), \quad (8)$$

where $K_a(\cdot, \cdot)$ and $K_b(\cdot, \cdot)$ are two kernels. Since $K_a(\cdot, \cdot)$ and $K_b(\cdot, \cdot)$ satisfy Mercer's conditions, all linear combinations are eligibles for kernels.

V. APPLICATION TO ENVISAT ASAR IMAGE

Let's summarize the procedure for oil slick detection:

- 1) SAR image I is composed into a multiscale representation that yields a vector with $2L + 1$ components: $(I^{\text{low}}, I_{L-1}^{\text{hori}}, I_{L-1}^{\text{vert}}, \dots, I_0^{\text{hori}}, I_0^{\text{vert}})^t$.
- 2) $\frac{M(M-1)}{2}$ SVMs are used to classify the observation into M classes by using a mixture of polynomial kernels (a standart and a texture kernel as defined in eq. (5) and (7)).

Since it is a supervised technique, region of interests (ROI) may be defined once and for all to characterize oil slicks, non-polluted sea, suspicious area and land for a given sea state and sensor.

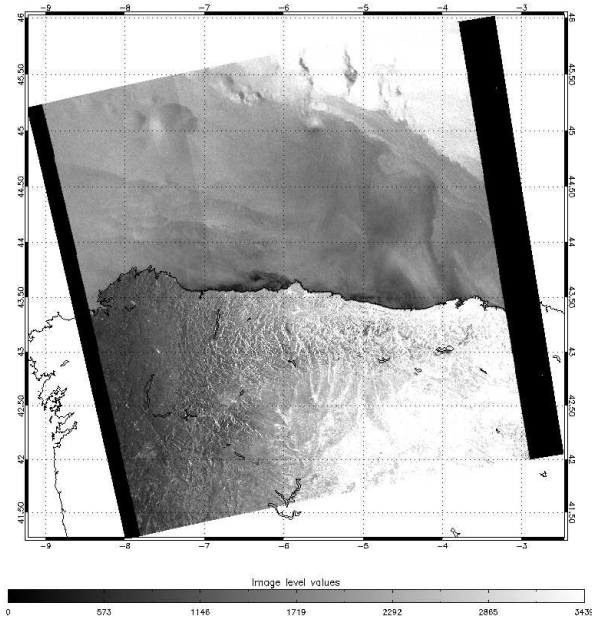


Fig. 2. ENVISAT ASAR image, December 9, 2002 acquired at 22h11 UTC (Wide Swath Mode, orbit 4063, polarization VV). Pixel size : 75 x 75 m. Total area : 468 x 445 km.

A. Prestige case

In 2002, the Prestige tanker accident off the Spanish coast was a major environmental disaster since a huge quantity of oil dumped in the ocean drifted over large distances. This example has been chosen for two main reasons: first, daily aircraft surveys were performed, giving maps of detected surface oil spills; second, many images were acquired over the region during the oil spill drift (ESA provided ENVISAT and ERS images over the area of the Prestige wreck for several months). Days and months after the Prestige accident, many oil spills were found near the Spanish and French coasts, difficulties were to find the oil spills in difficult atmospheric conditions and with degraded oil. Also, monitoring had to be done to predict the location of slick landings. The overall study is based on several areas of SAR images, but only a small example is illustrated in this paper. The SAR image presented here was acquired by ENVISAT over the north coast of Spain on December 9th 2002 at 22h11 UTC (Fig 2). The study area is on the coast (Fig. 3-a), showing dark patches with weak contrast and complex shapes, they could be oil spills or another phenomenon. In the following, the SVM techniques and a basic detection algorithm (smoothing followed by thresholding and Sobel filter) are applied on this study area, and then synergistic data are used to classify these dark patches. Then, results can be compared with aircraft tracking.

B. Detection

The basic algorithm (Fig. 3-b) detects well the main dark patches and is not confused with the coast. Fig. 3-c shows the result of the SVM techniques with four classes. Coast

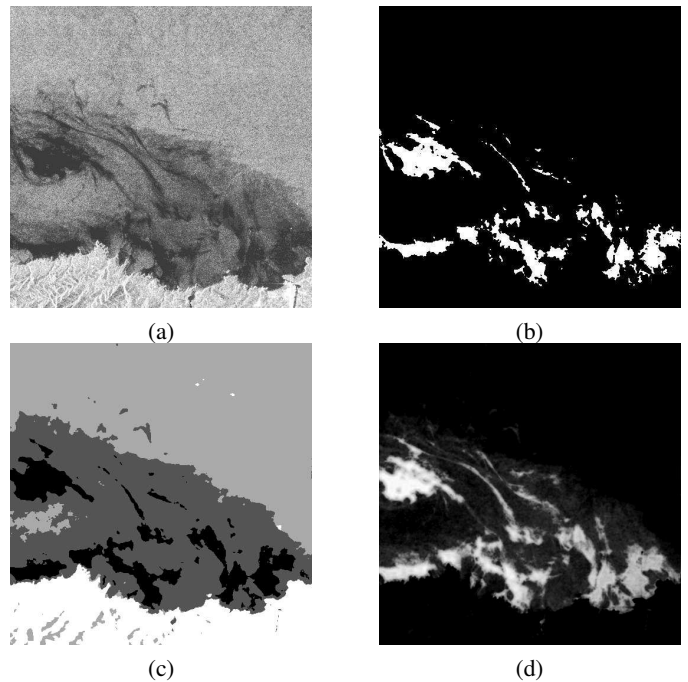


Fig. 3. (a) Study area extracted from Fig. 2, size : 38 x 38 km; (b) analysis of study area (a) using basic method. (c) Analysis of the study area (a) by using SVM technique; (d) soft-detection by using distance to hyperplane.

is well detected but mountains are confused (white and light grey Fig. 3-c), boats are marked in white over the sea. Main dark patches are detected in black, and a dark grey class is not classified. When the distance map is plotted (Fig. 3-d), more details appear, in particular the extensions of the spills to the north-west. Although coast is not well detected, the SVM method appears more interesting than the basic one since the number of classes determine several levels of sea surface roughness.

C. Discussion

To conclude about the nature of the dark patches, synergistic data are used to understand the atmospheric and oceanic conditions of this day. The weather was partly cloudy (visible and infrared radiation maps) with a south-easterly flux due to an atmospheric depression west of Spain (SeaWinds/QuikSCAT). The wind speed, directly inferred from the SAR image using the CMOD algorithm [25], is up to 14 ms^{-1} on the study area. Moreover, winds are offshore which implies that the dark area may correspond to weak winds due to an orographic effect. Waves conditions are calm (1 m significant wave height, calculated with Wave Watch III model). Sea surface temperature map (MODIS) does not show any upwelling in this area. These conditions imply that the main dark patches can be classified as pollution, which is confirmed by aircraft tracking maps (source: CEDRE) showing some pollution arriving this day on the coast. The extensions of the spill to the north-west are probably due to wind-induced drift. The dark grey zone is very likely linked to the weak wind area due to orographic effect. This image is a very difficult case for SAR pollution detection

because the study area is complex with many dark patches with different shapes, weak contrast, boats and coast. Moreover, environmental conditions show some conditions which can imply several interpretation of the dark patches.

VI. CONCLUSION

A supervised oil slick detection technique is proposed by using Support Vector Machines into a wavelet decomposition of a SAR image. A specific kernel is developed to perform accurate segmentation of local sea surface wave spectrum by using both radiometric and texture information.

Instead of previous studies, such as [26], this technique is efficient in an operational context and proved to be a relevant methodology to monitor pollution by oil slicks on the sea surface when used with synergistic data.

It is now necessary to assess the performances of this approach for different cases and to draw validity domains according to wind speed, sea state, oil characteristics and sensor.

ACKNOWLEDGMENT

Authors would like to thank ESA for the ERS, ENVISAT and Meteosat images; NOAA and NASA for SeaWinds/QuickSCAT, SeaWIFS, AVHRR, MODIS data and for the Wave Watch III model; and CEDRE (<http://www.le-cedre.fr>) for aircraft tracking maps. We also thank Vincent Kerbaol and Fabrice Collard (BOOST Technologies, France, <http://www.boost-technologies.com>) for the inferred wind speed from the SAR images using CMOD.

REFERENCES

- [1] T. Elfouhaily and B. Chapron, "A comparison of wind wave spectra used in ocean remote sensing modeling," in *Proc. of the IEEE IGARSS'96*, vol. 1, Lincoln, NE (USA), 27-31 May 1996, pp. 606-608.
- [2] B. Franklin, "On the stilling of waves by means of oil," *Philos. Trans.*, vol. 64, pp. 445-460, 1774.
- [3] W. Hühnerfuss and W. D. Garrett, "Experimental sea slicks: their practical applications and utilization for basic studies of air-sea interactions," *J. Geophys. Res.*, vol. 86, no. C1, pp. 439-447, 1981.
- [4] J. S. Scott, "The historical development of theories of wave-calming using oil," *Hist. Technol.*, vol. 3, pp. 163-186, 1978.
- [5] C. Marangoni, "Sul principio della viscosità superficiale dei liquidi stabilito," *Nuevo Cimento, ser. 2 (5/6)*, pp. 239-273, 1872.
- [6] W. Alpers and H. Hühnerfuss, "Radar signatures of oil films floating on the sea surface and the Marangoni effect," *J. Geophys. Res.*, vol. 93, no. C4, pp. 3642-3648, 1988.
- [7] —, "The damping of ocean waves by surface films: a new look at an old problem," *J. Geophys. Res.*, vol. 94, no. C5, pp. 6251-6265, 1989.
- [8] W. Hühnerfuss, W. Alpers, and W. L. Jones, "Measurements at 13.9 GHz of the radar backscattering cross section of the north sea covered with an artificial surface film," *Radio Sci.*, vol. 13, no. 6, pp. 979-983, 1978.
- [9] H. Hühnerfuss, W. Alpers, P. A. Lange, and W. Walter, "Attenuation of wind waves by artificial surface films of different chemical structures," *Geoph. Res. Lett.*, vol. 8, no. 11, pp. 1184-1186, 1981.
- [10] W. Hühnerfuss, W. Alpers, A. Cross, W. D. Garrett, W. C. Keller, P. A. Lange, W. J. Plant, F. Schlude, and D. L. Schuler, "The modification of X and L-band radar signals by monomolecular sea slicks," *J. Geophys. Res.*, vol. 88, no. C14, pp. 9817-9822, 1983.
- [11] J. W. Wright, "A new model for sea clutter," *IEEE Trans. Antennas Propagat.*, vol. 16, pp. 217-223, 1968.
- [12] M. Gade, W. Alpers, H. Hühnerfuss, V. Wismann, and P. Lange, "On the reduction of the radar backscatter by oceanic surface films: Scatterometer measurements and their theoretical interpretation," *Remote Sensing of Environment*, vol. 66, pp. 52-70, 1998.
- [13] M. Gade, J. Scholz, and C. von Viebahn, "On the detectability of marine oil pollution in European marginal waters by means of ERS SAR imagery," in *Proc. of the IEEE IGARSS'00*, vol. 6, Honolulu, HI (USA), 24-28 July 2000, pp. 2510-2512.
- [14] P. Lombardo, D. Conte, and A. Morelli, "Comparison of optimised processors for the detection and segmentation of oil slicks with polarimetric SAR images," in *Proc. of the IEEE IGARSS'00*, vol. 7, Honolulu, HI (USA), 24-28 July 2000, pp. 2963-2965.
- [15] Bjerde, A. H. S. Solberg, and R. Solberg, "Oil spill detection in SAR imagery," in *Proc. of the IEEE IGARSS'93*, vol. 3, Tokyo, Japan, 18-21 August 1993, pp. 943-945.
- [16] A. H. S. Solberg, G. Storvik, R. Solberg, and E. Volden, "Automatic detection of oil spills in ERS SAR images," *IEEE Trans. Geosci. Remote Sensing*, vol. 37, pp. 1916-1924, July 1999.
- [17] H. Espedal, "Detection of oil spill and natural film in the marine environment by spaceborne SAR," in *Proc. of the IEEE IGARSS'99*, vol. 3, Hamburg, Germany, 28 June, 2 July 1999, pp. 1478-1480.
- [18] M. Bertacca, F. Berizzi, E. Dalle Mese, and A. Capria, "A FARIMA-based analysis for wind falls and oil slicks discrimination in sea SAR imagery," in *Proc. of the IEEE IGARSS'04*, Anchorage, AK (USA), 20-24 Sept 2004.
- [19] S. Mallat, *A Wavelet Tour of Signal Processing*. Academic Press, 1998.
- [20] C. Kiecy and C. Lennard, "Unique reconstruction of band-limited signals by a Mallat-Zhong wavelet transform algorithm," *Fourier Analysis & Appl.*, vol. 3, no. 1, pp. 63-82, 1997.
- [21] C. J. Burges, "A tutorial on support vector machines for pattern recognition," in *Data mining and knowledge discovery*, U. Fayyad, Ed. Kluwer Academic, 1998, pp. 1-43.
- [22] V. N. Vapnick, *Statistical Learning Theory*. John Wiley and Sons Inc., 1998.
- [23] T. Joachims, "Making large-scale SVM learning practical," in *Advances in Kernel Methods - Support Vector Learning*, B. Schölkopf, C. Burges, and A. Smola, Eds. MIT-press, 1999, ch. 9, pp. 41-56, see also: <http://kernel-machines.org>.
- [24] G. Smits and E. Jordaana, "Improved SVM regression using mixtures of kernels," in *IJCNN*, 2002.
- [25] Y. Quilfen, B. Chapron, T. Elfouhaily, K. Katsaros, and J. Tournadre, "Observation of tropical cyclones by high resolution scatterometry," *J. Geophys. Res.*, vol. 103, no. C4, pp. 7767-7786, 1998.
- [26] G. Mercier, S. Derrode, W. Pieczynski, J.-M. Le Caillec, and R. Garello, "Multiscale oil slick segmentation with markov chain model," in *Proc. of the IEEE IGARSS'03*, Toulouse, France, July 21-25, 2003.